Nano Research

ISSN 1998-0124 CN 11-5974/O4
https://doi.org/10.1007/s12274-022-4970-6

Research Article

Well-structured 3D channels within GO-based membranes enable ultrafast wastewater treatment

Huaqiang Fu[1,§], Zhe Wang[2,3,§], Peng Li[2] (✉), Wei Qian[2], Zixin Zhang[1], Xin Zhao[2], Hao Feng[1], Zhugen Yang[4], Zongkui Kou[1,3] (✉), and Daping He[1,2] (✉)

[1] *School of Materials Science and Engineering, Wuhan University of Technology, Wuhan 430070, China*
[2] *Hubei Engineering Research Center of RF-Microwave Technology and Application, School of Science, Wuhan University of Technology, Wuhan 430070, China*
[3] *State Key Laboratory of Advanced Technology for Materials Synthesis and Processing, Wuhan University of Technology, Wuhan 430070, China*
[4] *School of Water, Energy and Environment, Cranfield University, Cranfield MK430AL, UK*
[§] *Huaqiang Fu and Zhe Wang contributed equally to this work.*

Received: 13 August 2022 / **Revised:** 22 August 2022 / **Accepted:** 25 August 2022

ABSTRACT

Graphene oxide (GO)-based membranes have been widely studied for realizing efficient wastewater treatment, due to their easily functionalizeable surfaces and tunable interlayer structures. However, the irregular structure of water channels within GO-based membrane has largely confined water permeance and prevented the simultaneously improvement of purification performance. Herein, we purposely construct the well-structured three-dimensional (3D) water channels featuring regular and negatively-charged properties in the GO/SiO_2 composite membrane via *in situ* close-packing assembly of SiO_2 nanoparticles onto GO nanosheets. Such regular 3D channels can improve the water permeance to a record-high value of 33,431.5 ± 559.9 $L \cdot m^{-2} \cdot h^{-1}$ (LMH) bar^{-1}, which is several-fold higher than those of current state-of-the-art GO-based membranes. We further demonstrate that benefiting from negative charges on both GO and SiO_2, these negatively-charged 3D channels enable the charge selectivity well toward dye in wastewater where the rejection for positive-charged and negative-charged dye molecules is 99.6% vs. 7.2%, respectively. The 3D channels can also accelerate oil/water (O/W) separation process, in which the O/W permeance and oil rejection can reach 19,589.2 ± 1,189.7 LMH bar^{-1} and 98.2%, respectively. The present work unveils the positive role of well-structured 3D channels on synchronizing the remarkable improvement of both water permeance and purification performance for highly efficient wastewater treatment.

KEYWORDS

graphene oxide, membranes, wastewater treatment, water channels, charge-selectivity

1 Introduction

The ever-growing global water scarcity and effluent discharge have made efficient and economic wastewater treatment an urgent task [1, 2]. The expected demands of wastewater (e.g., organic dye solutions and oil emulsions) for pollution-free emission or recycling utilization, have necessitated purification treatments that achieve pollutant elimination or retention of reusable solutes [3–5]. Many wastewater treatment processes have been developed, among which pressure driven membrane-based purification technology has attracted enormous attention due to its simplicity and low environmental impact [6]. However, both the inadequate water permeance and purification performance are hindering large scale application of existing membranes [7, 8].

Graphene oxide (GO)-based membranes with functionalizeable surfaces and adjustable interlayer structures have been demonstrated with great potential to realize high water permeance and good purification performance, thus capturing lots of interest in recent years [9, 10]. Specially, the water permeance of GO-based membranes was significantly enhanced by optimizing interlaminar water channels [11]. For example, water channels were improved by introducing zero-dimensional carbon dots inside GO membranes, several-fold increasing the water permeance from 53 to 439 $L \cdot m^{-2} \cdot h^{-1}$ (LMH) bar^{-1} [12]. Water channels of one-dimension established with nanotubes at interlayers of GO membranes can enhance the water permeance to about 700 LMH bar^{-1} [13, 14]. Furthermore, the water permeance of GO membranes with interlaminar two-dimensional water channels can be dramatically promoted to 4,536 LMH bar^{-1} [15]. Unfortunately, the generation rate of wastewater in one ordinary factory is still far beyond the processing efficiency provided by current GO-based membranes [16, 17]. The improvement bottleneck of water permeance in the GO-based membrane mainly derives from irregular water channels inside, which are randomly distributed and produced around three-dimensional (3D) voids of GO matrix [18]. Such irregular water channels can result in vast reservation of pristine confinements of GO interlayers [19, 20], where plugging can take place during water transport due to strong capillary force and the narrow nanochannels [13]. The well-structured 3D water channels are

Address correspondence to Peng Li, lipeng871120@whut.edu.cn; Zongkui Kou, zongkuikou@whut.edu.cn; Daping He, hedaping@whut.edu.cn

therefore highly desired to elevate the water permeance to a largest level, but their construction within GO membranes remains a crucial challenging.

Although promising in improving water permeability by constructing 3D water channels [21, 22], how to tradeoff the high water permeance and purification performance is another challenge [23, 24]. Theoretically, the purification mechanisms of the GO membrane include physical size sieving and electrostatic adsorbing toward specific solutes [25, 26]. The sieving is accomplished by microporous defects derived from imperfect stacking [27] and interlaminar confinement of GO nanosheets [28]. The 3D water channels will inevitably expand the pore diameters, resulting in a serious degradation on the purification capacity of GO membranes [29, 30]. Therefore, improving water permeance without sacrificing purification performance has become nearly impossible in conventionally designed membranes with 3D water channels.

In this work, we report the construction of regular and negatively-charged 3D water channels within GO membranes by *in situ* and close-packing growing of SiO_2 nanoparticles onto stacked GO nanosheets for synchronizing ultrahigh water permeance and purification performance. The water permeance of membrane with such well-structured 3D water channels can reach 33,431.5 ± 559.9 LMH bar^{-1}, which is a record-high value compared with the state-of-the-art membranes. Simultaneously, the negatively-charged 3D water channels are demonstrated to promote the charge selectivity of membranes toward dye molecules, in which the optimum rejections for positive-charged and negative-charged dye molecules are 99.6% and 7.2%, respectively. Besides, the 3D water channels can facilitate the oil/water (O/W) separation process, in which the O/W permeance and oil rejection can be boosted to 19,589.2 ± 1,189.7 LMH bar^{-1} and 98.2%, respectively.

2 Results and discussion

The regular and negatively-charged 3D water channels were constructed by assembling close-packing SiO_2 nanoparticles on stacked GO nanosheets, based on *in situ* hydrolysis strategy of tetraethyl orthosilicate (TEOS) (Fig. 1(a)) [31, 32]. Such well-structured SiO_2 nanoparticles can expand the micropores, and broaden the interlayer spacing to improve water permeability of the GO membrane. Moreover, the hydrophilic close-packing SiO_2 nanoparticles can facilitate water transport [33, 34]. Thus, we speculate that they can serve as 3D water channels. In contrast, water can hardly penetrate through pure GO membranes with tiny microporous and narrow interlayer spacing [35, 36], as depicted in Fig. 1(b), illustrating the crucial role of 3D water channels.

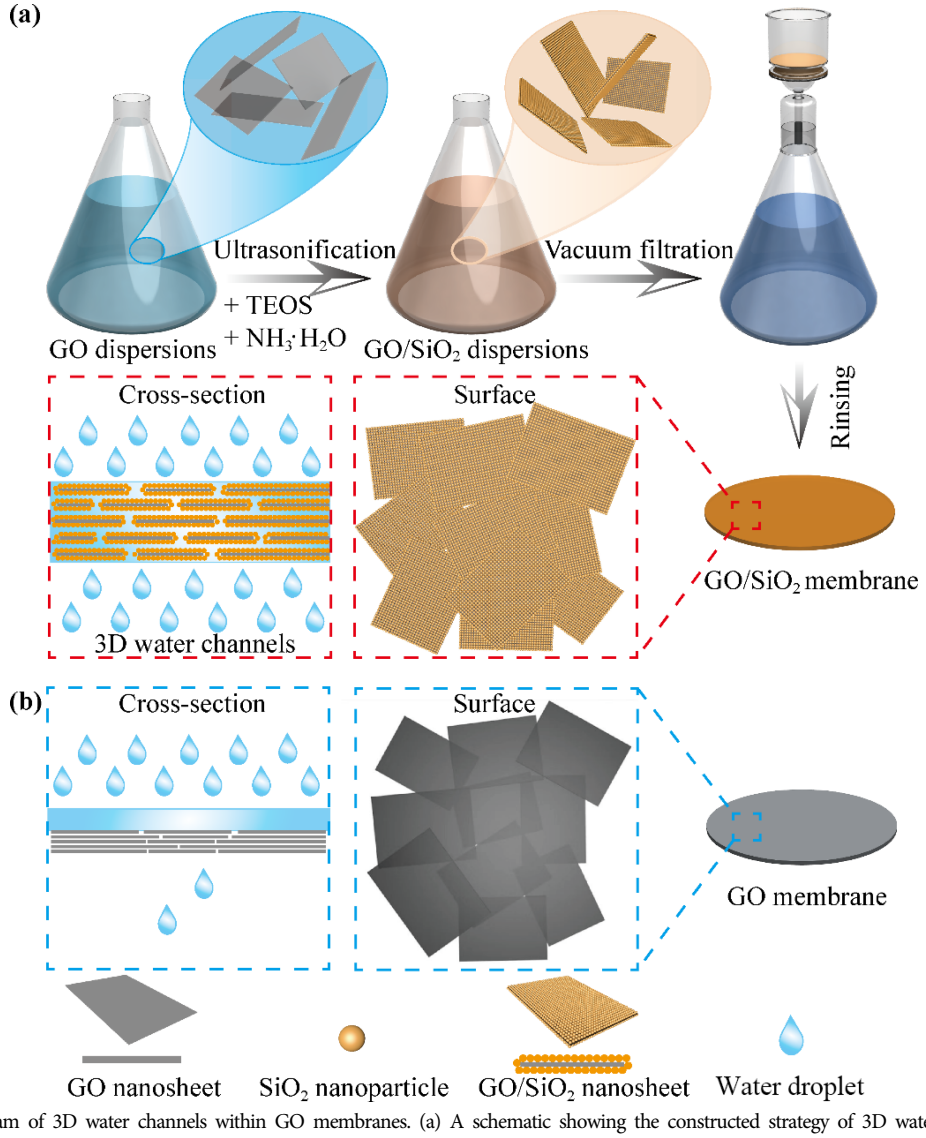

Figure 1 Design diagram of 3D water channels within GO membranes. (a) A schematic showing the constructed strategy of 3D water channels in GO/SiO_2 membranes, inserted with proposal models of surface and cross-sectional structures. (b) Schematic diagrams of surface and cross-sectional structures of GO membranes.

To obtain close-packing structure of SiO_2 nanoparticles on GO nanosheets, the growth behaviors were firstly investigated. We denote the dispersions and the as-prepared membranes as GO/SiO_2-*x*, where *x* (0, 0.1, 0.3, 0.5, 1.0, 2.0, and 3.0) represents the additive volume (mL) of TEOS. By tuning the value of *x*, the growth behavior of SiO_2 nanoparticles displays as two stages: irregular distribution and close-packing (Fig. 2(a)). Transmission electron microscopy (TEM) images of GO/SiO_2 dispersions confirm that the particle size (PS) and coverage rate (CR) of SiO_2 nanoparticles vary when altering the value of *x* (Fig. S1 in the Electronic Supplementary Material (ESM)). For $x = 0$, the pristine GO surface without any nanoparticles is set as the comparison template (Fig. 2(b)). Irregular distribution stage occurs when *x* values are below 0.5, featured by CR of SiO_2 nanoparticles beneath 100%, and slightly fluctuated PS (Figs. 2(c) and 2(d)). Notably, with *x* value exceeding 0.5, the CR reaches 100%, verifying the close-packing stage (Figs. 2(e)–2(g)). Further, the average PS dramatically increases from 15.44 to 60.86 nm, implying the controllable and optimizable structure in close-packing stage.

The abundant functional groups on GO nanosheets were confirmed by the intense O 1s peak in the X-ray photoelectron spectroscopy spectra of GO membranes (Fig. S2 in the ESM) and the equally distributed elemental mapping of O on the GO membrane surface (Fig. S3 in the ESM), which serve as the nucleation sites for *in situ* growth of SiO_2 nanoparticles [31, 32]. With the addition of TEOS dosage, the nucleation sites are gradually occupied by SiO_2 nanoparticles until completely filled to form close-packing structure (Figs. 2(b)–2(g) and Fig. S4 in the ESM). At the close-packing stage, these SiO_2 nanoparticles grow up rapidly due to lack of extra nucleation sites, conforming to the growth kinetics of colloid in sol-gel method [33].

GO/SiO_2-*x* membranes were fabricated on the mixed cellulose (MCE) substrates in vacuum-assisted self-assembly method, by using 0.5 mL GO/SiO_2-*x* dispersions (Fig. S5 in the ESM). Apparently, the *in situ* grown SiO_2 nanoparticles cannot deteriorate the membrane-forming ability (Figs. 3(a) and 3(b)), mainly resulted from the cross-linking of functional groups under hydrogen bond [34, 37]. When without SiO_2 nanoparticles, the pure GO membrane presents a dense and continuous surface (Fig. 3(c)). On the contrary, the surface becomes cracked gradually with the increasing contents of SiO_2 nanoparticles, especially at the close-packing process (Fig. S6 in the ESM). The fluffiest and most porous surface was obtained in the GO/SiO_2-2.0 membrane (Fig. 3(d)). In the cross-sectional scanning electron microscopy (SEM) image, GO/SiO_2-*x* membranes prepared by using 0.5 mL dispersions exhibit unquantifiable thickness and indistinguishable structure (Fig. S7 in the ESM). We thus increased the addition of GO/SiO_2-*x* dispersions to assemble thicker membranes. As depicted in Fig. 3(e), the pure GO membrane acquires the most compact stacking layers, producing narrow interlaminar water pathways. While the stacked structure of GO/SiO_2-2.0 membrane becomes remarkably fluffy (Fig. 3(f)), confirming the broadening of interlayer spacing. Moreover, the evenly distributed Si element certifies the interlinked SiO_2 nanoparticles on GO matrix (Fig. 3(g) and Fig. S8 in the ESM), which is consistent to our proposed scheme. The X-ray diffraction (XRD) patterns of GO/SiO_2-*x* membranes verify the crucial role of close-packing SiO_2 nanoparticles in constructing 3D water channels (Fig. 3(h)). The interlayer spacing is calculated to has a positive correlation with the addition volume of TEOS, and widens from 0.752 to 0.782 nm which is identified as the regular distribution stage ($x < 0.5$). The characteristic peak disappears at the close-packing stage ($x \geq 0.5$),

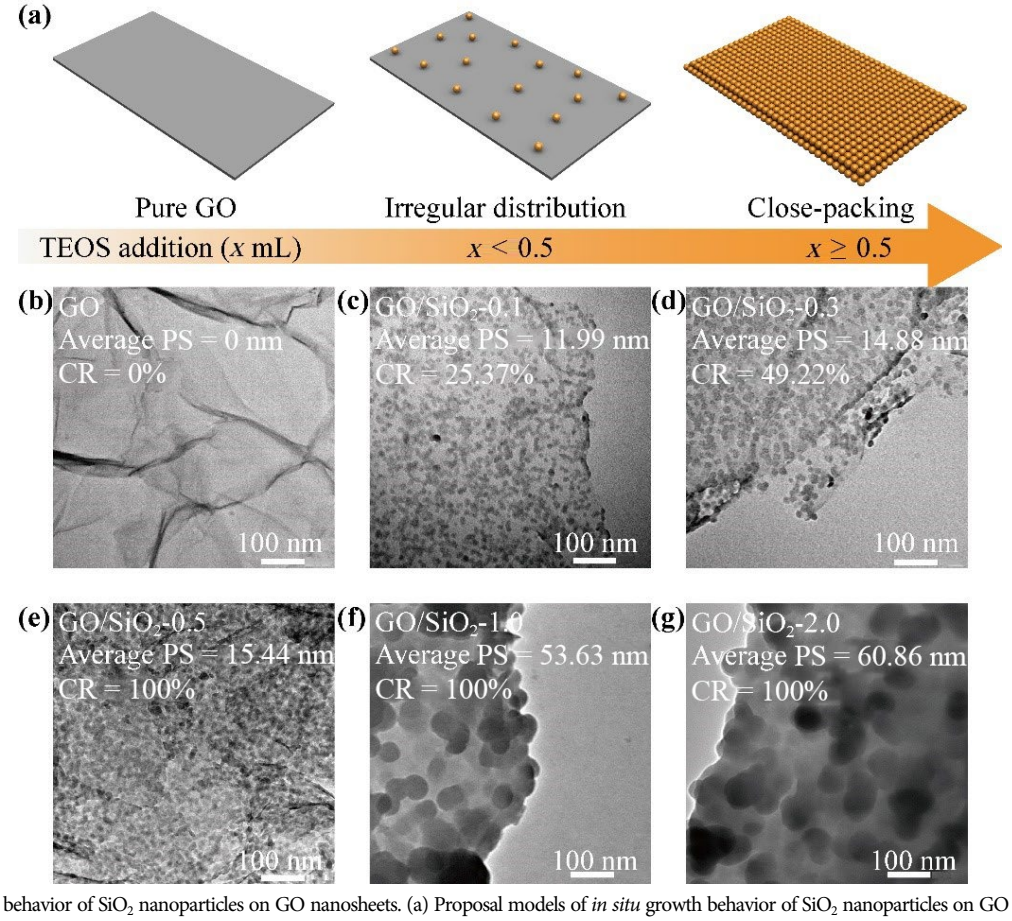

Figure 2 Growth behavior of SiO_2 nanoparticles on GO nanosheets. (a) Proposal models of *in situ* growth behavior of SiO_2 nanoparticles on GO nanosheets. (b)–(g) TEM images of GO/SiO_2-*x* dispersions ($x = 0$, 0.1, 0.3, 0.5, 1.0, and 2.0 corresponding (b), (c), (d), (e), (f), and (g)) showing the average PS and CR of SiO_2 nanoparticles.

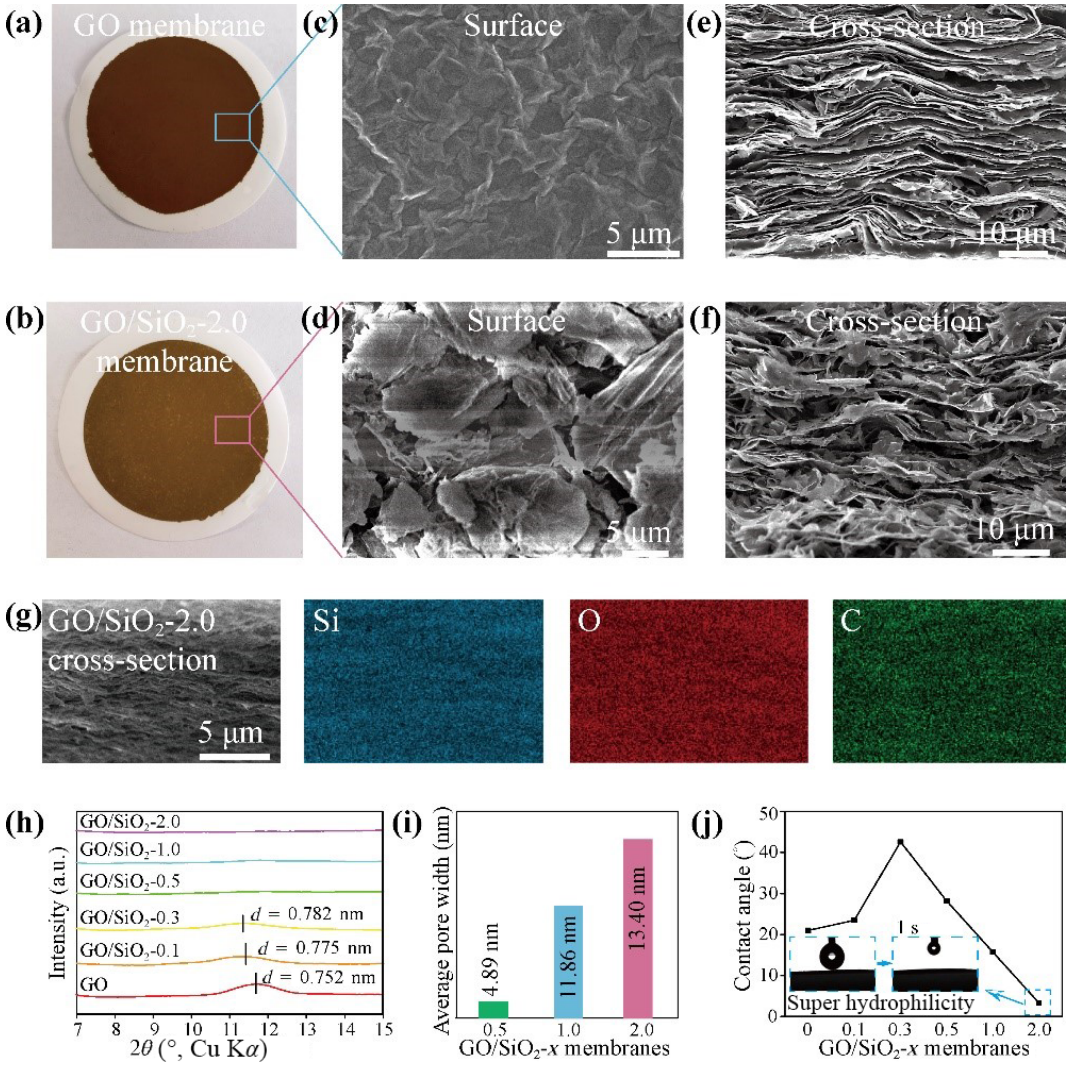

Figure 3 Structural characterizations of 3D water channels within GO membranes. Photos of (a) typical GO membrane and (b) GO/SiO_2-2.0 membrane. Surface SEM images of (c) typical GO membrane and (d) GO/SiO_2-2.0 membrane. Cross-sectional SEM images of (e) typical GO membrane and (f) GO/SiO_2-2.0 membrane. (g) Elemental mapping images of GO/SiO_2-2.0 membrane cross-section. (h) XRD patterns of GO/SiO_2-x (x = 0, 0.1, 0.3, 0.5, 1.0, and 2.0) membranes. (i) Average pore widths of GO/SiO_2-x membranes (x = 0.5, 1.0, and 2.0) with 3D water channels. (j) Contact angles of DI water on GO/SiO_2-x (x = 0, 0.1, 0.3, 0.5, 1.0, and 2.0).

which indicates complete elimination of periodic stacked lattice of GO nanosheets, affirming the construction of interlinked 3D water channels at this stage.

The average pore widths of GO/SiO_2-0.5, 1.0, and 2.0 membranes are 4.89, 11.86, and 13.40 nm, respectively (Fig. 3(i) and Fig. S9 in the ESM), verifying the controllable structure of 3D water channels by tuning the TEOS addition. Depending on TEOS dosage, the composite membrane also illustrates adjustable hydrophilicity as shown in Fig. 3(j). The variance of contact angle on membrane also matches well with the structure evolution of SiO_2 nanoparticles within membrane. At the irregular distribution stage (x < 0.5), the increase of contact angles mainly originates from reduction in the exposure level of hydrophilic functional groups. For the close-packing stage (x ≥ 0.5), the contact angle declines dramatically, confirming predominant correlation between structure of 3D water channels and hydrophilicity of membranes, supporting the crucial role of 3D water channels. We infer that the increased pore width of 3D water channels can afford improved capillary action to optimize hydrophilicity. Notably, the GO/SiO_2-2.0 membrane exhibits super hydrophilicity (Movie ESM1), in which the contact angle plunges from 15.4° to less than 3° within 1 s, which is conductive to high water permeability [38].

To explore the positive effect of 3D water channels on water permeable performance, water flux test was carried out under −0.08 MPa (Fig. 4(a)). As water channels are irregularly distributed (x < 0.5), the water permeance slightly increases beneath the order of 10^3 LMH bar^{-1}. With regular 3D water channels, the water permeance increases dramatically to 33,431.5 ± 559.9 LMH bar^{-1} in the GO/SiO_2-2.0 membrane (the extremely rapid water penetrant process can be seen in Movie ESM2), which is approximately three orders of magnitude improvement compared to pure GO membrane (40.6 LMH bar^{-1}). With further increasing x value to 3.0, the water permeance slightly declines to 32,464.2 LMH bar^{-1}, probably resulted from saturated growth of SiO_2 nanoparticles on GO nanosheets.

The GO/SiO_2-2.0 membrane with optimal 3D water channels was used for permeance stability test (Fig. 4(b)). During continuous filtering operation for 400 min, the water permeance stabilizes at an average of 33,332.7 LMH bar^{-1}, of which the variance is only 337.3. The outstanding stability of water permeance is originated from solid 3D water channels in the GO/SiO_2-2.0 membrane [39, 40]. As confirmed by zeta potential measurement (inset in Fig. 4(b)), the negative potentials SiO_2 nanoparticles help maintain the mesoporous structure of 3D water channels under pressure. Meanwhile the SiO_2 nanoparticles with multiple functional groups can crosslink with each other [31, 32], and immobilize on GO nanosheets [33, 34] for robust

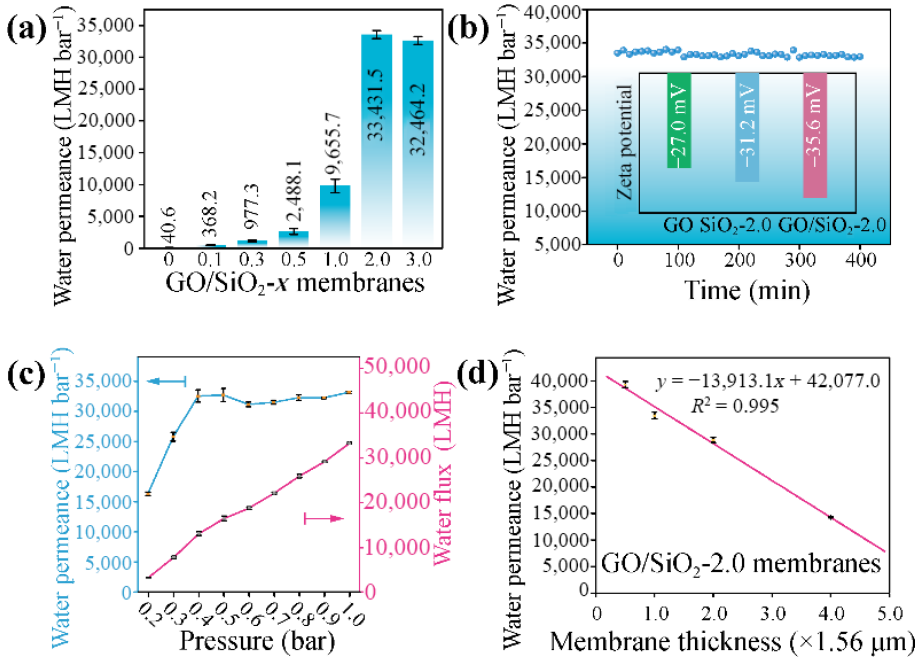

Figure 4 Water permeable performance measurements. (a) Water permeance of GO/SiO_2-*x* (*x* = 0, 0.1, 0.3, 0.5, 1.0, 2.0, and 3.0) membrane under −0.08 MPa. (b) Water permeance stability of the GO/SiO_2-2.0 membrane during continuous filtering operation for 400 min under −0.08 MPa, inserted with zeta potentials of GO dispersions, SiO_2-2.0 colloids, and GO/SiO_2-2.0 dispersions. (c) Water permeance and water flux of the GO/SiO_2-2.0 membrane under different pressures. (d) Water permeance of GO/SiO_2-2.0 membranes with multiplied thicknesses under −0.08 MPa.

construction of 3D water channels. With increasing filtering pressure, the stable water permeance and linearly augmented water flux confirm the solid structure of 3D water channels (Fig. 4(c)). Moreover, the fitting goodness between water permeance and membrane thickness reaches 0.995 (Fig. 4(d) and Fig. S10 in the ESM), also demonstrating the superiority and structure stability of regular 3D water channels.

For comparison, water permeance stability test of GO + SiO_2-2.0 membranes prepared by mechanical mixing of GO nanosheets and SiO_2-2.0 colloids was carried out (Fig. S11 in the ESM). To exclude the size effect, the close size and same content of SiO_2 nanoparticles in the preparation of both GO + SiO_2-2.0 and GO/SiO_2-2.0 membranes are applied (Fig. S12 in the ESM). The GO + SiO_2-2.0 membrane acquires a maximum water permeance of 4,269.5 LMH bar^{-1} (Fig. S13 in the ESM), which reaches the peak value of reported membranes prepared by mechanical mixing of GO and SiO_2 nanoparticles, confirming the data reliability in our work [41, 42]. But the permeance value promptly descends to 1,946.7 LMH bar^{-1} within 10 min. The characteristic XRD peak of GO demonstrates still existed GO interlayer spacing within GO + SiO_2-2.0 membrane (Fig. S14 in the ESM), leading to relatively low water permeance compared with GO/SiO_2-2.0 membranes (Fig. S15 in the ESM). Moreover, TEM images confirm the irregular distributed water channels within GO + SiO_2-2.0 membranes (Fig. S16 in the ESM), reflecting the crucial role of 3D water channels in improving membrane reliability.

Purification performance is another key index for membrane evaluation. In this work, we use three kinds of common industrial dye solutions to test [43], including methylene blue (MB), butyl rhodamine B (BRB), and methyl orange (MO). The membrane with 3D water channels can sustain significant charge-selectivity toward dye molecules (Fig. 5(a)). Specially, the rejections of GO/SiO_2-2.0 membranes toward positive-charged and negative-charged dye molecules are 99.6% and 7.2%, respectively. Besides, the GO/SiO_2-2.0 membrane with optimum 3D water channels exhibits unchanged MB rejections when dye volume is below 100 mL, verifying its reliability (Fig. 5(b)). Due to ultrahigh water permeability and excellent charge-selectivity toward dye molecules, the GO/SiO_2-2.0 membrane with optimal 3D water channels can be applied to highly efficient wastewater treatment, such as elimination of pollutants (Figs. 5(c) and 5(d)) or selective reservation of reusable solutes (Figs. 5(e) and 5(f)). In addition, the GO/SiO_2-2.0 membrane also displays excellent O/W separation performance. As shown in Fig. 5(g), diesel and soybean oil were prepared as oil emulsions to simulate emulsified oil in industrial wastewater. By using GO/SiO_2-2.0 membranes, the O/W permeance achieves 19,589.2 ± 1,189.7 LMH bar^{-1}, and the rejections of diesel and soybean oil emulsions exceed 99.0% and 98.2%, respectively (Fig. 5(h)).

Compared with representative GO-based membranes in the literature (Table S1 in the ESM), the GO/SiO_2-2.0 membrane with optimal 3D water channels exhibits a historically high water permeance, which is several-fold higher than the reported value (Fig. 5(i)). Synchronously, the optimal membrane reported in this work can maintain outstanding purification performance, validating the strategy feasibility and practicability of constructing 3D water channels within GO membranes.

The pore diameters of GO/SiO_2-2.0 membranes mainly distribute at the range from 30 to 100 nm (Fig. S9 in the ESM), which is extremely larger than the size of dye molecules [43]. Owing to expansion of the pore width, the MO rejection of GO/SiO_2-2.0 membranes deduces by half compared to pure GO membrane (Fig. 5(a)). Therefore, synchronizing high water permeance and excellent purification performance by constructing of 3D water channels in GO-based membranes is counterintuitive. The retention of excellent purification performance mainly results from enhanced negative surface potential by 3D water channels (inset in Fig. 4(b)). As shown in Fig. 6, the enhanced negative surface potential can promote electrostatic adsorption toward positive-charged dye molecules and repulsion to negative-charged dye molecules, respectively [44, 45]. Thus, the GO/SiO_2-2.0 membrane exhibits excellent dye separation performance under ultrahigh water flux. Moreover, the MB rejection of the GO/SiO_2-2.0 membrane plunges fastly when MB volume exceeds 100 mL (Fig. 5(b)), mainly resulted from electrostatic saturation [41], further confirming that the dye removal mechanism is based on

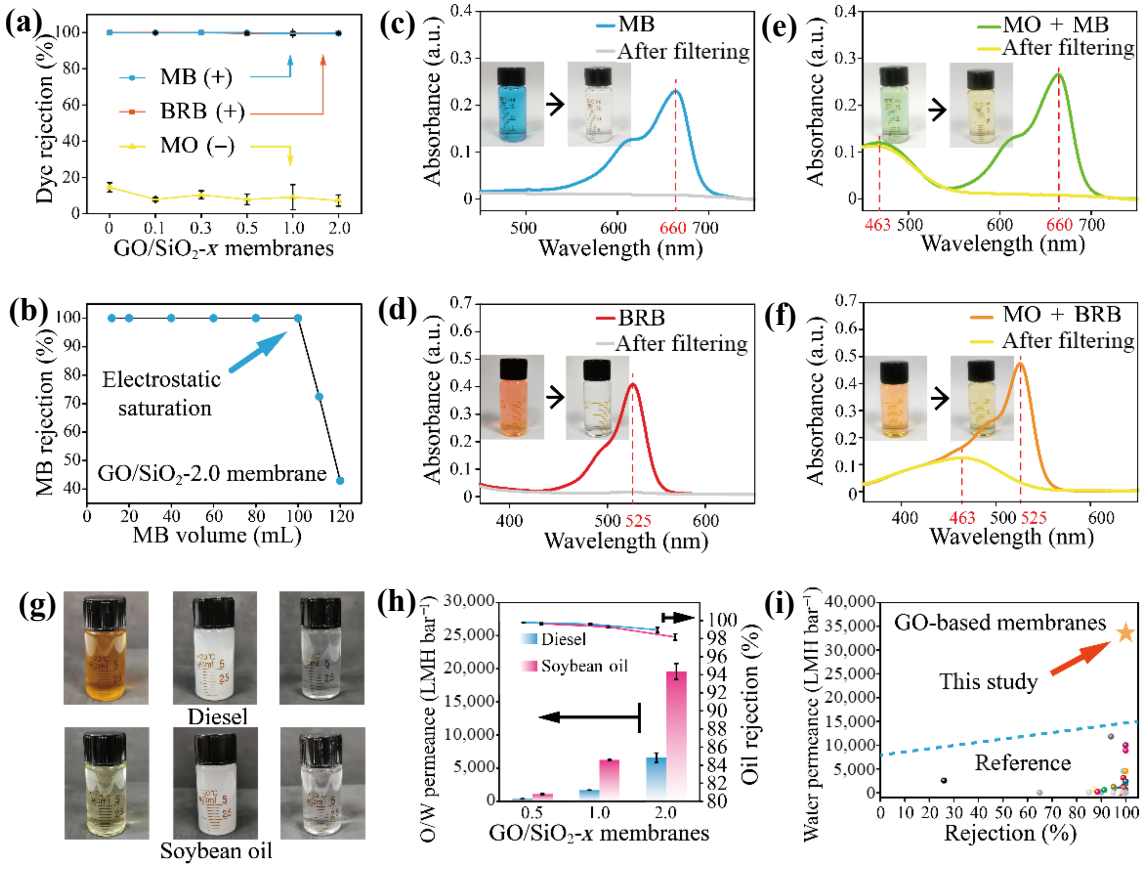

Figure 5 Purification performance measurement. (a) Dyes rejections of GO/SiO_2-x (x = 0, 0.1, 0.3, 0.5, 1.0, and 2.0) membranes toward MB, BRB, and MO. (b) MB rejections of the GO/SiO_2-2.0 membrane using increasing volumes of MB solutions under −0.08 MPa. UV spectrum and photographs of (c) MB and (d) BRB solution before and after filtering using the GO/SiO_2-2.0 membrane under −0.08 MPa. UV spectrum and photographs of mixing dyes solution containing (e) MO and MB and (f) MO and BRB before and after filtering using GO/SiO_2-2.0 membranes under −0.08 MPa. (g) Photographs of diesel, soybean oil, and their corresponding oil emulsions before and after filtering using the GO/SiO_2-2.0 membrane under −0.08 MPa. (h) O/W permeances and oil rejections of diesel and soybean oil using the GO/SiO_2-x (x = 0.5, 1.0, and 2.0) membrane under −0.08 MPa. (i) Comparison of water permeance and purification performance between the GO/SiO_2-2.0 membrane and the reported membranes in the literature (Table S1 in the ESM).

electrostatic reaction. In addition, benefiting from oil adsorbing of porous structure [46] and underwater oleophobic interface of SiO_2 nanoparticles [41, 47], the 3D water channels therefore improve the O/W separation efficiency.

3 Conclusions

In conclusion, we successfully addressed the challenge that achieving synchronous ultrahigh water permeance and purification performance in GO-based membranes, by constructing regular and negatively-charged 3D water channels through close-packing assembling of SiO_2 nanoparticles onto stacked GO nanosheets. The water permeance reaches a record-high value of 33,431.5 ± 559.9 LMH bar^{-1}, which is several-fold exceeding that of reported GO-based membranes. The ultrahigh water permeance can be maintained during continuous filtering operation for over 400 min, demonstrating the structural stability of such 3D water channels. Synchronously, the membrane with optimal 3D water channels can maintain outstanding charge selectivity toward dye molecules, in which the rejection of positive-charged and negative-charged dye molecules can achieve 99.6% and 7.2%, respectively. In addition, the 3D water channels can improve O/W separation efficiency, in which the O/W permeance and oil rejection can reach 19,589.2 ± 1,189.7 LMH bar^{-1} and 98.2%, respectively. These results validate the strategy feasibility of constructed regular and charged 3D water channels within GO membranes, offering great potential in the fields of highly efficient wastewater treatment.

4 Methods

4.1 Materials

GO (4.5 wt.%) was purchased from Wuhan Hanene Technology Co., Ltd. MCE substrates (diameter: 50 mm, pore size: 0.45 μm) were bought from Haining Guodian Taoyuan Medical Chemical Instrument Factory. TEOS and ammonium hydroxide ($NH_3 \cdot H_2O$) solution were obtained from Shanghai Macklin Biochemical Co., Ltd. All the other chemicals (alcohol, dyes, sodium dodecyl sulfate (SDS), etc.) used in this study were all purchased from Aladdin Industrial Co., Ltd.

4.2 Construction process of water channels in GO membranes

The construction of water channels was operated as follows. Firstly, deionized (DI) water and alcohol were mixed at the ratio of 1:19. Secondly, GO nanosheets were added into mixtures at a mass ratio of 2 mg·mL^{-1}, and the obtained dispersions were mixed and degassed in the mixing homogenizer of SK-300S11 (Shashin Kagaku Co., Ltd.). Thirdly, TEOS solution of x mL (x = 0, 0.1, 0.3, 0.5, 1.0, 2.0, and 3.0) was added into GO dispersions (50 mL) after adjusting the pH value to about 10 by $NH_3 \cdot H_2O$. Then, the GO/TEOS-x dispersions were ultrasonically treated for 3 h (at this stage SiO_2 nanoparticles *in situ* grew up on GO surface) to get GO/SiO_2-x dispersions. Finally, the GO/SiO_2-x membranes (Fig. S5 in the ESM) were obtained through vacuum-assisted self-assembly using 0.5 mL GO/SiO_2-x dispersions and 10 mL DI water.

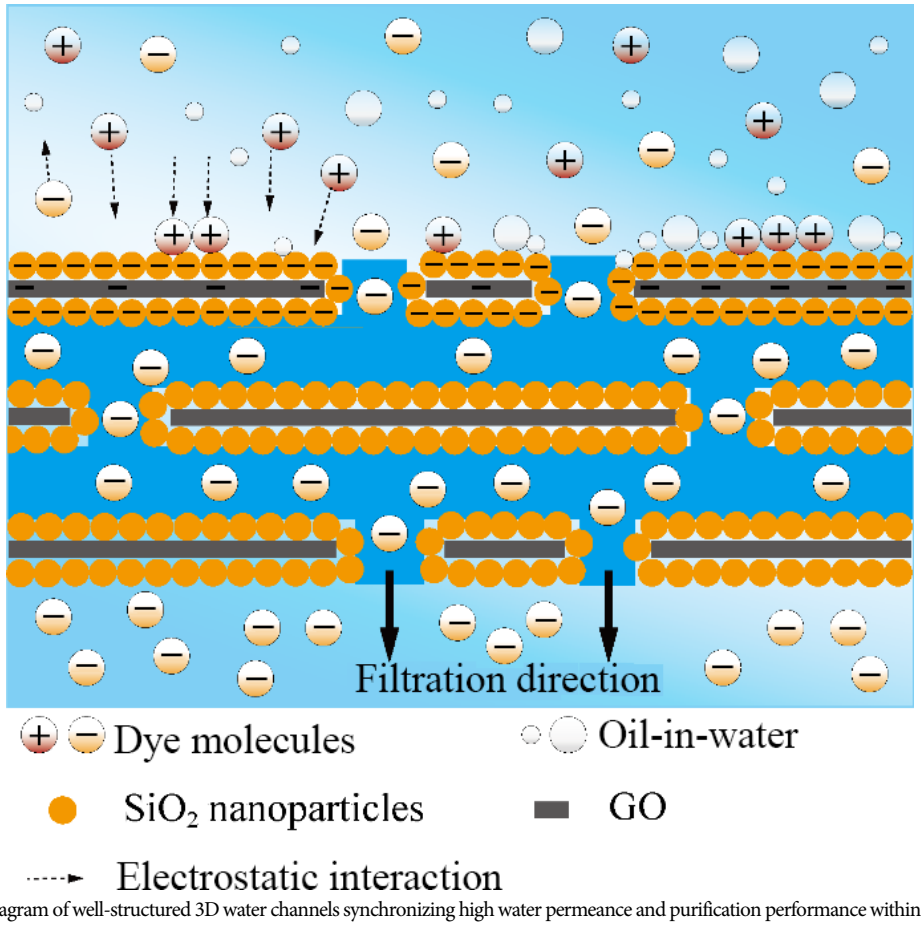

Figure 6 Mechanism diagram of well-structured 3D water channels synchronizing high water permeance and purification performance within GO membranes.

The GO + SiO_2-2.0 membrane was prepared based on mechanical mixing strategy. At first, SiO_2-2.0 colloid was prepared by ultrasonically hydrolyzing of 2.0 mL TEOS in mixture of 45 mL DI water and 5 mL alcohol for 3 h, of which the pH was adjusted to 10 by $NH_3{\cdot}H_2O$. Then GO was added into SiO_2-2.0 colloid at a mass ratio of 2 mg·mL^{-1} by ultrasonic mixing for 3 h to obtain GO + SiO_2-2.0 dispersions. Finally GO + SiO_2-2.0 membranes were prepared by vacuum-assisted self-assembly process using 0.5 mL GO + SiO_2-2.0 dispersion and 10 mL DI water. The prepared process can guarantee same contents of GO and SiO_2 particles in both GO + SiO_2-2.0 membrane and GO/SiO_2-2.0 membrane.

4.3 Characterization

Morphology and microstructure of GO/SiO_2-x membranes were characterized by SEM (JSM-7610F Plus), TEM (JEM-1400 Plus), and XRD (Rigaku Smartlab, Cu Kα). Element mapping was conducted using energy dispersive X-ray spectroscopy (EDS). Surface area and pore width of membranes were measured by Brunauer–Emmett–Teller (BET) surface area method using analyzing nitrogen sorption in a tristar-3020 instrument. Wet angles of water droplets on different membranes were measured in the automatic contact angle measuring instrument (OCA35). Ultraviolet/visible (UV) spectrophotometer (Shimadzu UV-1800) was utilized to collect UV spectra of different filtrates before and after filtering.

4.4 Concentration measurement of dye solutions and O/W emulsions

The dyes (MB, BRB, and MO) were all prepared with the concentration of 10 ppm, and O/W emulsions were prepared at the volume fraction of 0.5% by ultrasonically mixing SDS (0.1 g), oil (2.5 mL, diesel and soybean oil), and DI water (497.5 mL) for 6 h. Due to samples of dyes solutions or O/W emulsions with different concentrations show positive correlation to spectral intensity of UV absorption at their characteristic wavelength, the concentration of samples can be detected using UV spectrophotometer [38, 48]. As displayed in Figs. S17 and S18 in the ESM, the concentration and UV absorption intensity exhibit a good linear relationship with R-squared (R^2) value over 0.999. Hence, the concentration of dyes and oils can be determined according to the UV absorption intensity at their characteristic wavelengths.

4.5 Measurements of wastewater treatment performance

The water permeance, dye rejection, and oil removal performance were carried out on a home-made dead-end vacuum filtration device with the effective area of 12.56 cm^2 at room temperature. At first, all the membranes were rinsed by DI water for 3 min at −0.08 MPa to obtain stable flux value, then the water permeance (J) was calculated, as shown in Eq. (1). During measuring, all the collected data are averages of three samples during parallel tests.

$$J = \frac{\Delta V}{S.T.P} \tag{1}$$

where ΔV (L) is the volume of penetrant water, S (m^2) is the effective area of membranes, T (h) is the penetrant time, and P (bar) is the operating pressure.

Purification capacity is evaluated by rejection ratios of various dyes and O/W emulsions. The rejection ratios (R) can be computed according to Eq. (2)

$$R = \left(1 - \frac{C_b}{C_a}\right) \times 100\% \tag{2}$$

where C_b is the original concentration of filtrates before filtering, and C_a represents the concentration of filtrates after filtering.

Acknowledgements

The authors acknowledge financial support from UK NERC Fellowship (No. NE/R013349/2).

Electronic Supplementary Material: Supplementary material (photographs, TEM images of SiO_2 nanoparticles of GO/SiO_2-*x* dispersions, GO + SiO_2-2.0 dispersions, and SiO_2-2.0 colloids; surface SEM images, cross-sectional SEM images, elemental mapping images, and Brunauer–Emmett–Teller surface measurement results of GO/SiO_2-*x* membranes; water permeance, XRD patterns of GO + SiO_2-2.0 and GO/SiO_2-2.0 membranes. UV spectrum of dye solutions and corresponding concentration-absorbance function analysis, UV spectrum of oil emulsions and corresponding volume fraction-absorbance function analysis; performance comparisons of GO-based membranes in literatures; videos of wetting process of DI water on GO/SiO_2-2.0 membranes; videos of filtering process of GO/SiO_2-2.0 membranes under −0.08 MPa) is available in the online version of this article at https://doi.org/10.1007/s12274-022-4970-6.

References

[1] Mekonnen, M. M.; Hoekstra, A. Y. Four billion people facing severe water scarcity. *Sci. Adv.* **2016**, *2*, e1500323.

[2] Butler, E.; Hung, Y. T.; Al Ahmad, M.; Fu, Y. P. Treatment and management of industrial dye wastewater for water resources protection. In *Natural Resources and Control Processes*; Wang, L. K.; Wang, M. H. S.; Hung, Y. T.; Shammas, N. K. , Eds.; Springer International Publishing: Cham, 2016; pp 187–232.

[3] Grant, S. B.; Saphores, J. D.; Feldman, D. L.; Hamilton, A. J.; Fletcher, T. D.; Cook, P. L. M.; Stewardson, M.; Sanders, B. F.; Levin, L. A.; Ambrose, R. F. et al. Taking the "waste" out of "wastewater" for human water security and ecosystem sustainability. *Science* **2012**, *337*, 681–686.

[4] Jassby, D.; Cath, T. Y.; Buisson, H. The role of nanotechnology in industrial water treatment. *Nat. Nanotechnol.* **2018**, *13*, 670–672.

[5] Alvarez, P. J. J.; Chan, C. K.; Elimelech, M.; Halas, N. J.; Villagrán, D. Emerging opportunities for nanotechnology to enhance water security. *Nat. Nanotechnol.* **2018**, *13*, 634–641.

[6] Obotey Ezugbe, E.; Rathilal, S. Membrane technologies in wastewater treatment: A review. *Membranes* **2020**, *10*, 89.

[7] Shi, Z.; Zhang, W. B.; Zhang, F.; Liu, X.; Wang, D.; Jin, J.; Jiang, L. Ultrafast separation of emulsified oil/water mixtures by ultrathin free-standing single-walled carbon nanotube network films. *Adv. Mater.* **2013**, *25*, 2422–2427.

[8] Idris, S. N. A.; Jullok, N. Evaluation of commercial reverse osmosis and forward osmosis membranes at different draw solution concentration in pressure retarded osmosis process. *Mater. Today Proc.* **2021**, *46*, 2065–2069.

[9] Huang, H. B.; Ying, Y. L.; Peng, X. S. Graphene oxide nanosheet: An emerging star material for novel separation membranes. *J. Mater. Chem. A* **2014**, *2*, 13772–13782.

[10] Sun, M.; Li, J. H. Graphene oxide membranes: Functional structures, preparation and environmental applications. *Nano Today* **2018**, *20*, 121–137.

[11] Shen, J.; Liu, G. P.; Han, Y.; Jin, W. Q. Artificial channels for confined mass transport at the sub-nanometre scale. *Nat. Rev. Mater.* **2021**, *6*, 294–312.

[12] Wang, W. T.; Eftekhari, E.; Zhu, G. S.; Zhang, X. W.; Yan, Z. F.; Li, Q. Graphene oxide membranes with tunable permeability due to embedded carbon dots. *Chem. Commun.* **2014**, *50*, 13089–13092.

[13] Huang, H. B.; Song, Z. G.; Wei, N.; Shi, L.; Mao, Y. Y.; Ying, Y. L.; Sun, L. W.; Xu, Z. P.; Peng, X. S. Ultrafast viscous water flow through nanostrand-channelled graphene oxide membranes. *Nat. Commun.* **2013**, *4*, 2979.

[14] Gao, S. J.; Qin, H. L.; Liu, P. P.; Jin, J. SWCNT-intercalated GO ultrathin films for ultrafast separation of molecules. *J. Mater. Chem. A* **2015**, *3*, 6649–6654.

[15] Liu, Y. N.; Su, Y. L.; Guan, J. Y.; Cao, J. L.; Zhang, R. N.; He, M. R.; Gao, K.; Zhou, L. J.; Jiang, Z. Y. 2D heterostructure membranes with sunlight-driven self-cleaning ability for highly efficient oil-water separation. *Adv. Funct. Mater.* **2018**, *28*, 1706545.

[16] Bhol, P.; Yadav, S.; Altaee, A.; Saxena, M.; Misra, P. K.; Samal, A. K. Graphene-based membranes for water and wastewater treatment: A review. *ACS Appl. Nano Mater.* **2021**, *4*, 3274–3293.

[17] Keskin, B.; Ersahin, M. E.; Ozgun, H.; Koyuncu, I. Pilot and full-scale applications of membrane processes for textile wastewater treatment: A critical review. *J. Water Process Eng.* **2021**, *42*, 102172.

[18] Zhang, W. Y.; Xu, H.; Xie, F.; Ma, X. H.; Niu, B.; Chen, M. Q.; Zhang, H. Y.; Zhang, Y. Y.; Long, D. H. General synthesis of ultrafine metal oxide/reduced graphene oxide nanocomposites for ultrahigh-flux nanofiltration membrane. *Nat. Commun.* **2022**, *13*, 471.

[19] Zheng, K.; Li, S.; Chen, Z.; Chen, Y.; Hong, Y.; Lan, W. Highly stable graphene oxide composite nanofiltration membrane. *Nanoscale* **2021**, *13*, 10061–10066.

[20] Deng, H. H.; Zheng, Q. W.; Chen, H. B.; Huang, J.; Yan, H. D.; Ma, M. X.; Xia, M.; Pei, K. M.; Ni, H. G.; Ye, P. Graphene oxide/silica composite nanofiltration membrane: Adjustment of the channel of water permeation. *Sep. Purif. Technol.* **2021**, *278*, 119440.

[21] Feng, X. D.; Imran, Q.; Zhang, Y. Z.; Sixdenier, L.; Lu, X. L.; Kaufman, G.; Gabinet, U.; Kawabata, K.; Elimelech, M.; Osuji, C. O. Precise nanofiltration in a fouling-resistant self-assembled membrane with water-continuous transport pathways. *Sci. Adv.* **2019**, *5*, eaav9308.

[22] Yousefi, N.; Lu, X. L.; Elimelech, M.; Tufenkji, N. Environmental performance of graphene-based 3D macrostructures. *Nat. Nanotechnol.* **2019**, *14*, 107–119.

[23] Xu, Z. W.; Li, X. H.; Teng, K. Y.; Zhou, B. M.; Ma, M. J.; Shan, M. J.; Jiao, K. Y.; Qian, X. M.; Fan, J. T. High flux and rejection of hierarchical composite membranes based on carbon nanotube network and ultrathin electrospun nanofibrous layer for dye removal. *J. Memb. Sci.* **2017**, *535*, 94–102.

[24] Park, H. B.; Kamcev, J.; Robeson, L. M.; Elimelech, M.; Freeman, B. D. Maximizing the right stuff: The trade-off between membrane permeability and selectivity. *Science* **2017**, *356*, eaab0530.

[25] Liu, G. G.; Ye, H. Q.; Li, A. T.; Zhu, C. Y.; Jiang, H.; Liu, Y.; Han, K.; Zhou, Y. H. Graphene oxide for high-efficiency separation membranes: Role of electrostatic interactions. *Carbon* **2016**, *110*, 56–61.

[26] Hong, S.; Constans, C.; Surmani Martins, M. V.; Seow, Y. C.; Guevara Carrió, J. A.; Garaj, S. Scalable graphene-based membranes for ionic sieving with ultrahigh charge selectivity. *Nano Lett.* **2017**, *17*, 728–732.

[27] Seo, D. H.; Pineda, S.; Woo, Y. C.; Xie, M.; Murdock, A. T.; Ang, E. Y. M.; Jiao, Y. L.; Park, M. J.; Lim, S. I; Lawn, M. et al. Anti-fouling graphene-based membranes for effective water desalination. *Nat. Commun.* **2018**, *9*, 683.

[28] Boukhvalov, D. W.; Katsnelson, M. I.; Son, Y. W. Origin of anomalous water permeation through graphene oxide membrane. *Nano Lett.* **2013**, *13*, 3930–3935.

[29] Aba, N. F. D.; Chong, J. Y.; Wang, B.; Mattevi, C.; Li, K. Graphene oxide membranes on ceramic hollow fibers-microstructural stability and nanofiltration performance. *J. Memb. Sci.* **2015**, *484*, 87–94.

[30] Lai, G. S.; Lau, W. J.; Goh, P. S.; Ismail, A. F.; Yusof, N.; Tan, Y. H. Graphene oxide incorporated thin film nanocomposite nanofiltration membrane for enhanced salt removal performance. *Desalination* **2016**, *387*, 14–24.

[31] Li, J.; Cui, J. C.; Yang, J. Y.; Ma, Y.; Qiu, H. X.; Yang, J. H. Silanized graphene oxide reinforced organofunctional silane composite coatings for corrosion protection. *Prog. Org. Coatings* **2016**, *99*, 443–451.

[32] Chen, S. L.; Dong, P.; Yang, G. H.; Yang, J. J. Kinetics of formation of monodisperse colloidal silica particles through the hydrolysis and condensation of tetraethylorthosilicate. *Ind. Eng. Chem. Res.* **1996**, *35*, 4487–4493.

[33] Zhou, X.; Shi, T. J. One-pot hydrothermal synthesis of a mesoporous

SiO_2-graphene hybrid with tunable surface area and pore size. *Appl. Surf. Sci.* **2012**, *259*, 566–573.

[34] Kou, L.; Gao, C. Making silicananoparticle-covered graphene oxide nanohybrids as general building blocks for large-area superhydrophilic coatings. *Nanoscale* **2011**, *3*, 519–528.

[35] Xu, W. L.; Fang, C.; Zhou, F. L.; Song, Z. N.; Liu, Q. L.; Qiao, R.; Yu, M. Self-assembly: A facile way of forming ultrathin, high-performance graphene oxide membranes for water purification. *Nano Lett.* **2017**, *17*, 2928–2933.

[36] Yang, Q.; Su, Y.; Chi, C.; Cherian, C. T.; Huang, K.; Kravets, V. G.; Wang, F. C.; Zhang, J. C.; Pratt, A.; Grigorenko, A. N. et al. Ultrathin graphene-based membrane with precise molecular sieving and ultrafast solvent permeation. *Nat. Mater.* **2017**, *16*, 1198–1202.

[37] Zhuravlev, L. T. The surface chemistry of amorphous silica. Zhuravlev model. *Colloids Surf. A Physicochem. Eng. Asp.* **2000**, *173*, 1–38.

[38] Wang, Z.; Mao, B. Y.; Zhao, M.; Calatayud, D. G.; Qian, W.; Li, P.; Hu, Z. G.; Fu, H. Q.; Zhao, X.; Yan, S. L. et al. Ultrafast macroscopic assembly of high-strength graphene oxide membranes by implanting an interlaminar superhydrophilic aisle. *ACS Nano* **2022**, *16*, 3934–3942.

[39] Zhang, W. H.; Yin, M. J.; Zhao, Q.; Jin, C. G.; Wang, N. X.; Ji, S. L.; Ritt, C. L.; Elimelech, M.; An, Q. F. Graphene oxide membranes with stable porous structure for ultrafast water transport. *Nat. Nanotechnol.* **2021**, *16*, 337–343.

[40] Ritt, C. L.; Werber, J. R.; Deshmukh, A.; Elimelech, M. Monte Carlo simulations of framework defects in layered two-dimensional nanomaterial desalination membranes: Implications for permeability and selectivity. *Environ. Sci. Technol.* **2019**, *53*, 6214–6224.

[41] Liu, Y.; Zhang, F. R.; Zhu, W. X.; Su, D.; Sang, Z. Y.; Yan, X.; Li, S.; Liang, J.; Dou, S. X. A multifunctional hierarchical porous SiO_2/GO membrane for high efficiency oil/water separation and dye removal. *Carbon* **2020**, *160*, 88–97.

[42] Sun, J. W.; Bi, H. C.; Su, S.; Jia, H. Y.; Xie, X.; Sun, L. T. One-step preparation of GO/SiO_2 membrane for highly efficient separation of oil-in-water emulsion. *J. Memb. Sci.* **2018**, *553*, 131–138.

[43] He, Y. C.; Yang, J.; Kan, W. Q.; Zhang, H. M.; Liu, Y. Y.; Ma, J. F. A new microporous anionic metal-organic framework as a platform for highly selective adsorption and separation of organic dyes. *J. Mater. Chem. A* **2015**, *3*, 1675–1681.

[44] Ranjan, P.; Verma, P.; Agrawal, S.; Rao, T. R.; Samanta, S. K.; Thakur, A. D. Inducing dye-selectivity in graphene oxide for cationic dye separation applications. *Mater. Chem. Phys.* **2019**, *226*, 350–355.

[45] Bhattacharyya, A.; Ghorai, S.; Rana, D.; Roy, I.; Sarkar, G.; Saha, N. R.; Orasugh, J. T.; De, S.; Sadhukhan, S.; Chattopadhyay, D. Design of an efficient and selective adsorbent of cationic dye through activated carbon-graphene oxide nanocomposite: Study on mechanism and synergy. *Mater. Chem. Phys.* **2021**, *260*, 124090.

[46] Bi, H. C.; Xie, X.; Yin, K. B.; Zhou, Y. L.; Wan, S.; He, L. B.; Xu, F.; Banhart, F.; Sun, L. T.; Ruoff, R. S. Spongy graphene as a highly efficient and recyclable sorbent for oils and organic solvents. *Adv. Funct. Mater.* **2012**, *22*, 4421–4425.

[47] Junaidi, N. F. D.; Othman, N. H.; Fuzil, N. S.; Mat Shayuti, M. S.; Alias, N. H.; Shahruddin, M. Z.; Marpani, F.; Lau, W. J.; Ismail, A. F.; Aba, N. F. D. Recent development of graphene oxide-based membranes for oil-water separation: A review. *Sep. Purif. Technol.* **2021**, *258*, 118000.

[48] Scherer, M. D.; Oliveira, S. L.; Lima, S. M.; Andrade, L. H. C.; Caires, A. R. L. Determination of the biodiesel content in diesel/biodiesel blends: A method based on fluorescence spectroscopy. *J. Fluoresc.* **2011**, *21*, 1027–1031.